Field-induced condensation of π to 2π soliton lattices in chiral magnets

M. Winter, A. Pignedoli, Marein C. Rahn, Aleksandr S. Sukhanov, B. Achinuq, J. R. Bollard, M. Azhar, K. Everschor-Sitte, D. Pohl, S. Schneider, A. Tahn, V. Ukleev, M. Valvidares, A. Thomas, D. Wolf, P. Vir, T. Helm, G. van der Laan, T. Hesjedal, J. Geck, C. Felser, B. Rellinghaus

Angaben zur Veröffentlichung / Publication details:

Winter, M., A. Pignedoli, Marein C. Rahn, Aleksandr S. Sukhanov, B. Achinuq, J. R. Bollard, M. Azhar, et al. 2026. "Field-induced condensation of π to 2π soliton lattices in chiral magnets." *Communications Physics* 9 (1): 264. https://doi.org/10.1038/s42005-026-02785-3.

communications physics
A Nature Portfolio journal

Article

https://doi.org/10.1038/s42005-026-02785-3

Field-induced condensation of π to 2π soliton lattices in chiral magnets

M. Winter[1,2,3] ✉, A. Pignedoli[4], M. C. Rahn[5,6], A. S. Sukhanov[5,6], B. Achinuq[7], J. R. Bollard[7,8], M. Azhar[4], K. Everschor-Sitte[4], D. Pohl[2], S. Schneider[2], A. Tahn[2], V. Ukleev[9], M. Valvidares[10], A. Thomas[3,6], D. Wolf[3], P. Vir[1], T. Helm[11], G. van der Laan[8], T. Hesjedal[7,8], J. Geck[6,12], C. Felser[1,12] & B. Rellinghaus[2] ✉

Chiral soliton lattices (CSLs) emerge from the competition between Dzyaloshinskii–Moriya interaction, anisotropy, and magnetic fields. While well established in monoaxial helimagnets, their role in materials with anisotropic, direction-dependent chirality remains poorly understood. Here, we report the direct observation of a crossover from π to 2π soliton lattices in the non-centrosymmetric Heusler compound $Mn_{1.4}PtSn$. Combining Lorentz transmission electron microscopy, resonant elastic X-ray scattering, and micromagnetic simulations, we identify a π-CSL as the magnetic ground state—rather than the expected spiral phase—which evolves into a classical 2π-CSL under increasing out-of-plane fields. This transition is governed by an interplay between uniaxial magnetocrystalline anisotropy and magnetostatic interactions, qualitatively captured by a double sine-Gordon model. Our framework extends to materials with D_{2d}, S_4, C_{nv}, or C_n symmetries in the thin-film limit, providing a unifying route to engineer magnetic phase diagrams in chiral systems with implications for soliton-based spintronics and topological transport.

Topologically nontrivial spin textures, such as (anti)skyrmions and chiral soliton lattices (CSLs), can arise in magnetic systems where symmetric exchange, the asymmetric Dzyaloshinskii–Moriya interaction (DMI), and magnetocrystalline magnetostatic interactions compete under external magnetic fields. In most known cases, such as monoaxial chiral helimagnets like $Cr_{1/3}NbS_2$, $Cr_{1/3}TaS_2$, or $Yb(Ni_{1-x}Cu_x)_3Al_9$, CSLs emerge from a helical ground state stabilized by isotropic DMI and easy-plane anisotropy[1–3]. There, the soliton wave vector aligns along a single hard axis. Recently, increased attention has turned to magnets with planar anisotropic DMI, particularly in non-centrosymmetric systems such as $Mn_{1.4}PtSn$[4], which host a rich variety of magnetic textures including antiskyrmions[5–8]. In these systems, the DMI favors opposite chirality along orthogonal directions in the crystallographic *ab* plane, enabling nontrivial two-dimensional textures with strong dependence on sample shape[9–11]. However, the microscopic mechanisms governing field-driven transitions between these textures, and the question whether CSL-like states can arise as distinct ground states, remain poorly understood.

The relevance of soliton lattices extends well beyond magnetic systems. Analogous periodic topological structures occur in the physics of elementary particles, in particular in quantum chromodynamics[12–14], where they describe modulated chiral condensates, and in nematic liquid crystals, where related field-theoretical models capture defect lattices and director modulations[15,16]. As in magnetic systems, field-driven transitions between such lattices, including the formation of topologically protected skyrmionic structures, play a central role in the underlying physics.

In the present work, we focus on the emergence of CSLs in $Mn_{1.4}PtSn$, a compound with D_{2d} symmetry and planar anisotropic DMI. While prior work has largely emphasized skyrmionic textures, we demonstrate that the magnetic ground state of $Mn_{1.4}PtSn$ films is not a helical spiral, but rather a stripe domain structure composed of alternating domains separated by π

[1]Max Planck Institute for Chemical Physics of Solids, Dresden, Germany. [2]Dresden Center for Nanoanalysis, cfaed, TUD University of Technology Dresden, Dresden, Germany. [3]Leibniz Institute for Solid State and Materials Research Dresden, Dresden, Germany. [4]Faculty of Physics and Center for Nanointegration Duisburg-Essen (CENIDE), University of Duisburg-Essen, Duisburg, Germany. [5]Experimental Physics IV, Center for Electronic Correlations and Magnetism, University of Augsburg, Augsburg, Germany. [6]Institute for Solid State and Materials Physics, TUD University of Technology Dresden, Dresden, Germany. [7]Department of Physics, Clarendon Laboratory, University of Oxford, Oxford, UK. [8]Diamond Light Source, Didcot, UK. [9]Helmholtz-Zentrum Berlin für Materialien und Energie, Berlin, Germany. [10]ALBA Synchrotron Light Source, Barcelona, Spain. [11]Dresden High Magnetic Field Laboratory (HLD-EMFL), Helmholtz-Zentrum Dresden-Rossendorf, Dresden, Germany. [12]Würzburg-Dresden Cluster of Excellence ct.qmat, TUD University of Technology Dresden, Dresden, Germany.
✉e-mail: moritz.winter2@tu-dresden.de; bernd.rellinghaus@tu-dresden.de

Bloch walls, effectively a π-CSL. Upon increasing the out-of-plane magnetic field, this ground state continuously evolves into a conventional CSL with 2π solitons. To uncover this transition, we combine Lorentz transmission electron microscopy (LTEM), resonant elastic X-ray scattering (REXS), and micromagnetic simulations. The field-tunable evolution of modulation length and harmonic content reveals a soliton condensation process governed by a delicate interplay of magnetocrystalline anisotropy (MCA) and magnetostatic (MS) interactions. Our experimental results are supported by micromagnetic simulations, which reveal the importance of MS interactions in achieving quantitative agreement with the data. A double sine-Gordon model accounts for the qualitative features of both the π- and 2π-CSL configurations and the crossover between them.

Importantly, this behavior is not unique to $Mn_{1.4}PtSn$. Our framework applies broadly to systems with anisotropic DMI and uniaxial anisotropy, including materials with D_{2d}, S_4, C_{nv}, and C_n point group symmetries[17], as well as thin films of cubic chiral magnets under strain. This establishes a generalized route to soliton lattice formation and control in a wide range of magnetic materials, with implications for spintronic functionality, topological transport, and related fields of physics.

Results and discussion

Experimental approach

High-quality single crystals of $Mn_{1.4}PtSn$ were grown by the self-flux method, as previously reported in ref. 18. A thin lamella (19 μm × 14.7 μm × 80 nm) with a *c*-axis surface normal was cut from an oriented single crystal by focused ion beam (FIB) milling. As illustrated in Figs. 1a, b, our experimental strategy is based on complementary insights in real and momentum space. Thickness and shape variations of FIB-prepared lamellae make it crucial to perform these measurements on the very same specimen. To achieve this, the lamella was mounted on top of an X-ray opaque molybdenum disc (3mm diameter, 50 μm thickness) with an 8 × 8 μm^2 quadratic aperture that fits both commercial TEM holders and a dedicated sample carrier designed for our REXS experiments (see "Methods" section).

Figure 1c shows the LTEM contrast of the magnetic ground state of $Mn_{1.4}PtSn$ in zero magnetic field at room temperature. The image reveals two domains with stripe-type features that alternate periodically along the crystallographic *a* and *b* axes[4–6]. In the corresponding REXS pattern in Fig. 1d, the magnetic scattering originating from the two perpendicular domain variants is combined to form a pseudo four-fold magnetic diffraction pattern. As indicated in the figure, the observed Bragg peaks are labeled $q_{i,\xi}$, where i indicates the i^{th} harmonic of the periodic stripe pattern and ξ refers to domains whose stripes alternate along either the *a* or *b* crystallographic axis of the sample.

Upon applying an out-of-plane magnetic field along the crystallographic *c* axis ($\boldsymbol{H}_{\text{ext}}||c$) as exemplified in Fig. 1e for a field of $H_{\text{ext}} = 300$ mT, the LTEM patterns change significantly: (i) The modulation length $L_{\text{LTEM}}(H_{\text{ext}})$ is increased with respect to the patterns observed in zero field. (ii) The contrast modulation becomes asymmetric. Regions of homogeneous contrast grow wider, while neighboring regions with an alternating contrast become smaller. This indicates a broadening of stripes with a uniform out-of-plane component of the magnetization like in field-polarized (i.e., out-of-plane magnetized) regions that are separated by narrowed stripes of modulated (in-plane) magnetization such as in domain walls (DWs).

These findings are corroborated by the results of our complementary REXS experiments. As shown in Fig. 1d, f, the magnitude of the magnetic scattering vector $q_{i,x}(H_{\text{ext}}) = 2\pi/L_{\text{REXS}}(H_{\text{ext}})$ is reduced upon increasing the field. The field-induced occurrence of additional harmonics, i.e., the 2^{nd} harmonics $q_{2,a}$ and $q_{2,b}$, and their field-dependent intensities reflect the asymmetric change of the modulation of the underlying magnetic structures already observed in the LTEM images.

Analyzing the nature of the chiral soliton lattices from real space magnetic imaging

In order to better understand the magnetic textures underlying the observed stripe patterns and their field-induced modification, we first analyze the LTEM images in more detail. The transport of intensity equation (TIE)[19–21] is used to calculate the phase Φ of the electron wave from the intensity distribution in the LTEM images. Then, if the electrostatic potential of the sample is constant across the considered area, variations of the projected in-plane magnetic induction $\vec{B}$ can be determined from this phase according to

$$\begin{aligned} \partial_x\Phi(\vec{r}) &= \tfrac{e}{\hbar}\int B_y(\vec{r}_\perp, z)dz = \tfrac{e}{\hbar}\bar{B}_y t\,, \\ \partial_y\Phi(\vec{r}) &= -\tfrac{e}{\hbar}\int B_x(\vec{r}_\perp, z)dz = -\tfrac{e}{\hbar}\bar{B}_x t\,. \end{aligned} \tag{1}$$

Here, e, $\hbar$, $\bar{B}_x$, $\bar{B}_y$, and t denote the electron charge, Planck's constant, and the *x* and *y* components of the projected magnetic induction along *z* throughout the thickness of the sample, respectively. The latter was determined right after the ion beam cutting in the FIB to be $t \lesssim 100$ nm. To ensure that any likewise determined modulations of the phase solely arise from local variations of the in-plane magnetic induction in the sample, we restrict our considerations to small areas of the carefully cut lamella, for which a homogeneous thickness can be assumed and phase variations originating from the electrostatic potential of the sample can thus be neglected. Figure 2a–c show the resulting maps of the magnetic phase shift for one variant of stripe patterns acquired in out-of-plane magnetic fields, μ_0H_{ext}, of 0, 150, and 300 mT. At zero magnetic field (Fig. 2a) the phase pattern consists of stripes of alternating bright and dark contrast. As the gradient contrast represents strength and sign of Φ, according to Eq. (1), in-plane magnetic induction occurs solely at the interfaces between stripes of alternating contrast, since only here, the gradient is non-zero. Also, the direction of this induction is opposite for changes of contrasts at the stripe borders from bright to dark and from dark to bright pointing along the positive and negative *x* direction, respectively. This shows that the DWs bordering the stripe domains are 180° (π) Bloch walls. It is apparent from the phase patterns that with increasing field, the dark stripes widen on the expense of the bright ones. Since with increasing field, the sample is successively magnetized along the field direction, the dark stripes can be identified as domains with a (constant) out-of-plane magnetization in positive *z* direction. At sufficiently high magnetic fields, the width of the bright domains magnetized opposite to field direction, d_1, shrinks to just the DW width, w. At this point, each two neighboring 180° (π) Bloch walls combine to form a single 360° (2π) DW.

These conclusions, which are solely drawn from the experimentally acquired LTEM images, enable us to deduce the underlying spin textures and their modulation along the direction of the contrast modulation, referred to as the propagation direction. In Figs. 2g–i schematic pictures of textures are shown for fields of 0, 150, and 300 mT. At zero magnetic field [Fig. 2g], compensated up and down magnetized domains of roughly equal widths ($d_1 \simeq d_2$) are separated by π Bloch walls of width w, thereby forming a stripe domain pattern. The DWs are of right-handed chirality as defined with respect to the propagation direction along the positive *x* axis. The resulting magnetic texture compares to that of neighboring out-of-plane magnetized stripe domains. In contrast to conventional stripe domains, however, these stripe domains form a *periodic lattice* of well defined periodicity. Accordingly, and in order to account for the connecting π DWs, we refer to this magnetic ground state as π-CSL.

Upon increasing the field, domains magnetized in field direction start to grow at the expense of those magnetized opposite to the field [$d_2 > d_1$, see Fig. 2h], while w, which is fixed by the exchange constants (see below), remains largely constant. At $\mu_0H_{\text{ext}} = 300$ mT, only domains magnetized along the field remain ($d_2 > d_1 = 0$), and pairs of neighboring 180° (π) Bloch walls coalesce to form solitonic 360° (2π) DWs of width $2w$ [Fig. 2i]. This spin texture resembles closely that of a conventional CSL.

In order to validate the likewise deduced 1D spin textures, they were extended along the *x* direction to form 2D stripes, based on which both, phase images and maps of the in-plane magnetic induction, B_y, were then calculated using the `Ubermag` sub-package `mag2exp`[22] following the scheme of Beleggia and Zhu[23]. As can be seen from a comparison of the images in Fig. 2a–f with those in Fig. 2j–o, the experimental and the model-

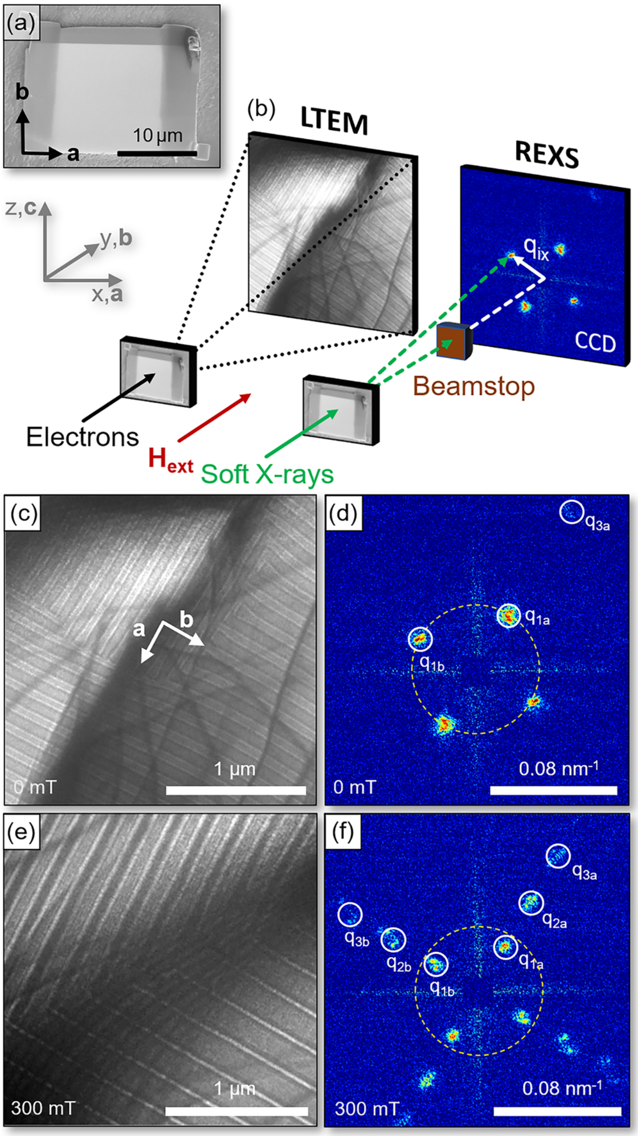

Fig. 1 | Experimental setup and basic experimental findings. a Scanning electron microscopy (SEM) image of the $Mn_{1.4}PtSn$ lamella mounted across the square hole of a Mo carrier disc. **b** Geometries of the Lorentz transmission electron microscopy (LTEM) and resonant elastic X-ray scattering (REXS) experiments performed in transmission on the very same sample with magnetic fields applied along the direction of the impinging electron and X-ray beam, respectively. LTEM images and REXS patterns acquired at zero field and 300mT are shown in (**c**–**f**). The LTEM images in (**c**, **e**) were acquired at an overfocus of 288 µm. They reveal two perpendicularly oriented domains with stripy contrasts that alternate periodically along the crystallographic a and b axes of the $Mn_{1.4}PtSn$ lamella. The intensity of the background-subtracted REXS patterns in (**d**, **f**) is presented on a logarithmic color scale. The dashed yellow circle indicates the inverse modulation length in zero field, $q(\mu_0 H_{ext} = 0)$. Note that the diagonally oppositely lying third-harmonic peak (q_{3a}) [expected in the lower-left quadrant of (**d**)] falls outside the active area of the in-vacuum CCD detector and is therefore not captured in the recorded image.

derived phase images and induction patterns are in very good agreement thereby confirming the deduced texture models.

Aside from the d_2/d_1 disproportion, the applied field also increases the modulation length in a characteristic way. Figure 3 shows this modulation length as determined from both LTEM, L_{LTEM}, and REXS, L_{REXS}, together with the LTEM-derived widths of the stripe domains, $d_1 + w$ and $d_2 + w$, as function of the applied field. The modulation lengths determined independently in two different experiments on the very same sample coincide perfectly. Both, L_{LTEM} and L_{REXS} grow monotonically with increasing field, and diverge upon approaching magnetic saturation in the ferromagnetically polarized state. The dashed vertical line in Fig. 3 indicates the field, where d_1 vanishes and each two neighboring 180° (π) Bloch walls coalesce to form a 2π soliton each. As this marks the transition from a π-CSL to a conventional CSL, we refer to this field as H_{CSL} with $\mu_0 H_{CSL} \simeq 226mT$. Above H_{CSL}, we find $d_1 + w \approx w = 46$ nm. Hence, the width of a 2π soliton in $Mn_{1.4}PtSn$ is $2w = 92$ nm.

The reciprocal space signature of the CSL from REXS experiments

The accompanying REXS experiments are summarized in Fig. 4. Fig. 4a shows the field dependence of the magnitude of the scattering vector as determined from the 1st order magnetic Bragg reflections (Fig. 1) normalized to their values at $H_{ext} = 0$ along the crystallographic a and b axes $q(H_{ext})_{1,a}$ and $q(H_{ext})_{1,b}$, i.e., for both observed domain variants. We refer to this vector as the propagation vector of the chiral spin modulation. As revealed in Fig. 3, the increase in periodic length (i.e., the inverse of the magnitude of the propagation vector) is identical for both domains. The steepest decrease in $q(H_{ext})$ and increase in $L(H_{ext})$ occurs at fields above $\mu_0 H_{ext} = \mu_0 H_{CSL}$, i.e., in the stability range of the conventional CSL.

The REXS experiments also support the finding from our LTEM analysis that the magnetic ground state in $Mn_{1.4}PtSn$ is a π-CSL rather than the helical phase. Figure 4b shows the field dependence of the normalized intensities $I_{i,a/b}(H_{ext})/I_{1,a/b}(0)$ of the 1st, 2nd, and 3rd harmonic of the propagation vector as determined from the 1st, 2nd, and 3rd order magnetic Bragg reflections. While for the sinusoidal spin modulation of a helical phase, only the fundamental spatial frequency (i.e., the 1st order reflection) is expected to occur with a monotonically decreasing intensity, also higher harmonics are observed that even exhibit non-monotonic field dependencies. At low fields, the REXS pattern contains only the 1st and 3rd harmonics, while the 2nd harmonic sets only in above around 30 mT. Its intensity increases and reaches its maximum at 260 mT. Specifically, the behavior of the 3rd harmonic, which is found to vanish at intermediate fields around 150 mT and then to rise again until all intensities are suppressed upon reaching full saturation in the ferromagnetic state, contradicts a continuous sinusoidal modulation. It is rather typical for a more discontinuous Heaviside or boxcar type of modulation with unequally long up and down segments. Similar non-sinusoidal modulations and DW sharpening effects have been observed in multilayered magnetic systems, where higher harmonics and soliton coalescence play a role[15]. Then, multiples of the nth harmonic are suppressed when the ratio of up to down segments is $\frac{1}{n} / \frac{(n-1)}{n}$. For the 3rd harmonic, this would relate to a ratio of the widths of up and down domains of $d_2/d_1 = 1/2$, which according to the LTEM analyses is fulfilled below roughly 140 mT (Fig. 2). A similar behavior is observed, e.g., in stripe domains of ferromagnetic multilayers[24].

Theoretical validation and simulations

The non-centrosymmetric half-Heusler compound $Mn_{1.4}PtSn$ can be described by a continuum micromagnetic model with D_{2d} symmetry. The total micromagnetic energy is

$$\mathcal{H} = \int d^3\boldsymbol{r}\left[\epsilon_{ex} + \epsilon_{DMI} + \epsilon_{Zeeman} + \epsilon_{MCA} + \epsilon_{MS}\right], \tag{2}$$

with

$$\begin{aligned} \epsilon_{ex} &= A(\nabla \boldsymbol{m})^2, \\ \epsilon_{DMI} &= D\left(m_z\partial_x m_y - m_y\partial_x m_z - m_x\partial_y m_z + m_z\partial_y m_x\right), \\ \epsilon_{Zeeman} &= -\mu_0 M_s \boldsymbol{m}\cdot\boldsymbol{H}_{ext}, \\ \epsilon_{MCA} &= -K_{MCA}(\boldsymbol{m}\cdot\hat{z})^2, \\ \epsilon_{MS} &= -\frac{1}{2}\mu_0 M_s \boldsymbol{m}\cdot\boldsymbol{H}_{MS}(\boldsymbol{m}), \end{aligned} \tag{3}$$

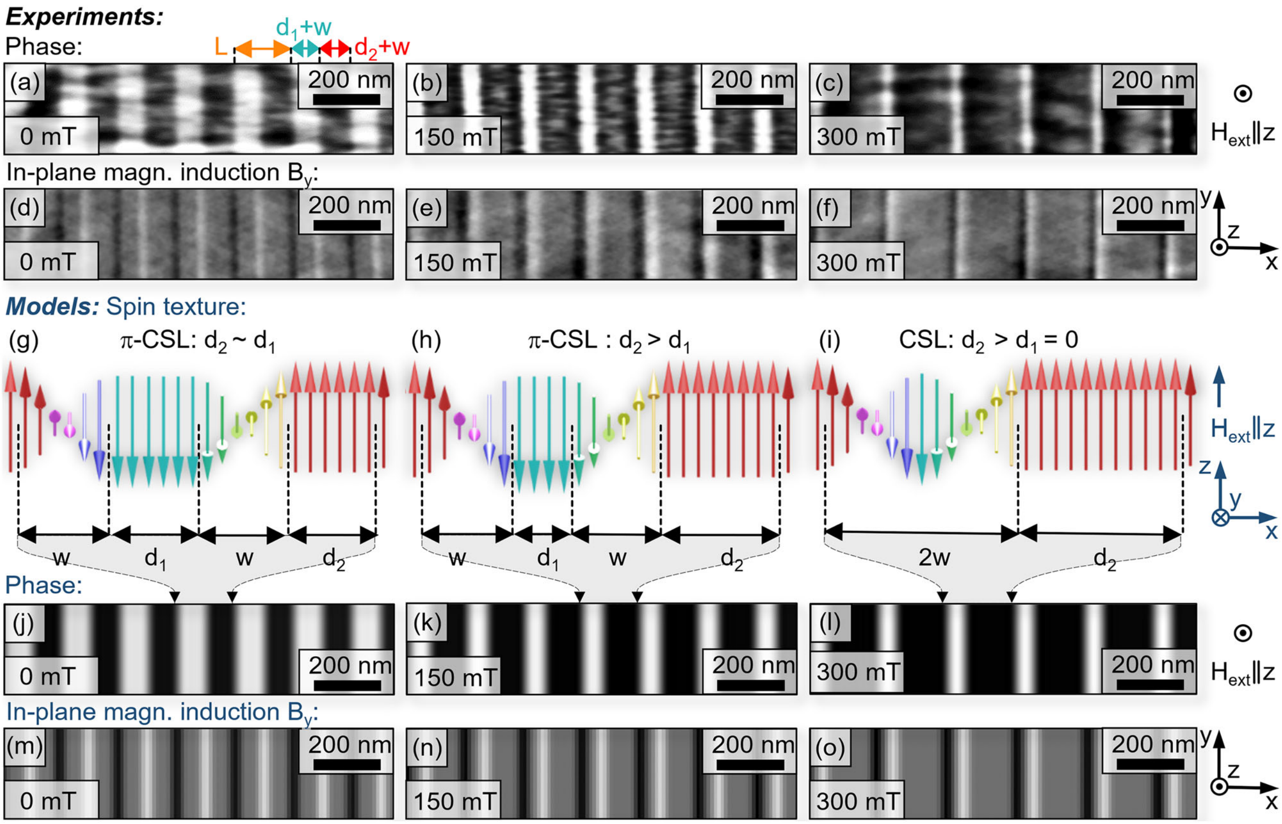

Fig. 2 | Real-space spin-texture analysis from Lorentz transmission electron microscopy (LTEM) phase imaging. Stripe contrast observed by LTEM in out-of-plane magnetic fields, $\mu_0 H$, of 0, 150, and 300mT. **a–c** Maps of the magnetic phase shift imposed on the electron wave as derived from transport-of-intensity equation (TIE) analyses of the LTEM images for sections of the stripe patterns. For this representation, all phase patterns were rotated within the *xy* viewing plane to align the direction of alternating contrast with the abscissa, which is identified as *x* direction, the magnetic field is applied along the *z* direction. Colored arrows indicate the periodic length, L_{LTEM}, and the widths of bright and dark stripe domains, d_1 and d_2, respectively (each including the domain wall width, *w*). **d–f** Maps of the *y* component of the in-plane magnetic induction, B_y, derived from the phase maps using Eq. (1). **g–i** Spin textures deduced from the induction maps and from the measures derived from phase maps assuming domain walls (DWs) with right-handed chirality, as discussed in the subsection "Analyzing the nature of the chiral soliton lattices from real space magnetic imaging". Corresponding phase and B_y maps as calculated from the model spin textures in (**g–i**) are shown in (**j–l**) and (**m–o**), respectively. All phase and induction patterns are qualitative images that are contrast-enhanced for better visibility.

representing the energy densities due to the symmetric exchange interaction, the D_{2d} symmetry DMI[17,25,26], the Zeeman interaction, the uniaxial MCA, and the MS interaction, respectively. Interactions are taken into account up to the second order in spin-orbit coupling. *A* is the ferromagnetic exchange stiffness, *D* the strength of the DMI, $\boldsymbol{m}$ the unit vector field describing the magnetization direction, μ_0 the vacuum magnetic permeability, M_s the saturation magnetization and $\boldsymbol{H}_{\mathrm{ext}}$ the strength of the external magnetic field. The uniaxial anisotropy with strength $K_{\mathrm{MCA}} > 0$ favors magnetization along the $\hat{z}$ direction. The MS interaction is included via the MS field $\boldsymbol{H}_{\mathrm{MS}}(\boldsymbol{m})$ [27].

The D_{2d} symmetry DMI favors opposite-handed helical twisting along the two perpendicular directions *x* and *y*, which manifests itself in the different LTEM contrast of the stripes in domains with perpendicular propagation directions in Figs. 1c, e. For $Mn_{1.4}PtSn$, the crystallographic *a*, *b*, and *c* axes correspond to *x*, *y*, and *z* directions in Eq. (3), respectively, where *z* is oriented along the film normal. Because $Mn_{1.4}PtSn$ exhibits easy-axis anisotropy, its spin modulation differs from that of CSLs in monoaxial helimagnets, which possess easy-plane (uniaxial) magnetic anisotropy.

MS interactions are known to play a crucial role in the $Mn_{1.4}PtSn$ samples considered here, and are therefore treated fully within micromagnetic simulations (see the Methods subsection "Computational Methods"). To gain initial insight into the physics underlying the observed stripe contrast, we first reduce Eqs. (2) and (3) to an effective one-dimensional model and approximate the MS interactions to lowest order by an effective anisotropy term. This approach enables us to construct a qualitative phase diagram as discussed below.

Magnetic phase diagram of $Mn_{1.4}PtSn$. To gain some qualitative insight into the physics of the stripe domains, we first describe the various magnetic interactions within a double sine-Gordon (dSG) model. To this end, we approximate the MS interactions by replacing ϵ_{MCA} and ϵ_{MS} in Eq. (3) by the effective uniaxial anisotropy density $\epsilon_{\mathrm{ani}}^{\mathrm{eff}} = \epsilon_{\mathrm{MCA}} + \epsilon_{\mathrm{MS}} = -\tilde{K}(\boldsymbol{m}\cdot\hat{z})^2$ with an effective anisotropy constant $\tilde{K} = K_{\mathrm{MCA}} - K_{\mathrm{MS}}$. $\tilde{K}$ is reduced with respect to the magneto-crystalline anisotropy alone by $K_{\mathrm{MS}} = \mu_0 N M_s^2/2$, which represents the shape anisotropy of the ferromagnetic medium with *N* being the demagnetization factor.

Motivated by the LTEM results, we adopt a coplanar spin-spiral ansatz for the magnetization, confined to the *yz*-plane and propagating along the *x*-direction: $\boldsymbol{m} = (0, -\sin\phi(x), \cos\phi(x))$, where $\phi(x)$ is the local azimuthal angle of the magnetization. Substituting this ansatz into Eq. (2) and minimizing the resulting energy functional with respect to ϕ yields the dSG equation (for details see Supplementary Note 1, "Qualitative model with anisotropy replacement", and Fig. S1, which illustrates the helical, π-CSL, and 2π-CSL solutions in the respective limiting cases), the solutions of which determine the magnetic phase diagram[28–30]. Figure 5 shows the resulting phase diagram for $Mn_{1.4}PtSn$, expressed in terms of the dimensionless field $h = 2\mu_0 M_s A H_{\mathrm{ext}}/D^2$ and anisotropy constant $\kappa = 2A\tilde{K}/D^2$. The diagram captures the emergence of the π-CSL and 2π-CSL phases as well as the crossover between them at $h = 2\kappa$[28,30].

In the field-dominated region $h > 2\kappa$ (green area), the 2π-CSL is stabilized, whereas in the anisotropy-dominated region $h < 2\kappa$ (blue area), the π-CSL resides. The black line denotes the phase boundary to the ferromagnetically saturated state, reached at the critical field $h_c(\kappa)$. The normalized MCA κ_{MCA}, calculated from $K_{\mathrm{MCA}} = 1 \times 10^5$ J m^{-3} [5], is indicated by the right dashed gray line. Experimentally, we observe the π-to-2π-CSL crossover at $h_{\mathrm{CSL}} \approx h_c/2$, i.e., roughly half the saturation field, which together with the measured h_c allows us to extract κ_{exp} (left dashed gray line). The resulting κ_{exp} is substantially smaller than κ_{MCA}, which is understood within the anisotropy replacement approximation: the MS interaction contributes a shape anisotropy K_{MS} of opposite sign to K_{MCA}, reducing the effective anisotropy and thus placing the system within the CSL stability region, as illustrated by the green arrow. Only in the limiting case where the MS term fully compensates the MCA (i.e., $K \to 0$) would the dSG model reduce to a single sine-Gordon model and a helical state would re-emerge as the ground state.

This qualitative conclusion is supported by the frequent experimental observations of a pronounced thickness dependence of the emerging magnetic textures in $Mn_{1.4}PtSn$, for which the modulation length of the periodic arrangement of magnetic stripe domains is found to increase with increasing sample thickness[6,9,10,31]. With increasing sample thickness the demagnetization factor and thus the shape anisotropy is reduced and accordingly, the effective anisotropy $\tilde{K}$ increases. This agrees very well with the predictions of the dSG where the modulation length of the CSL is indeed expected to grow with increasing anisotropy (see Supplementary Note 2, "Variation of the modulation length with anisotropy"), until it finally diverges upon transforming into the ferromagnetic state[32–34].

From Fig. 5 it can be seen that in zero external magnetic field, the transition from a CSL to the ferromagnetic state occurs at an effective dimensionless anisotropy of roughly $\kappa \simeq 1.2$. This value corresponds to a

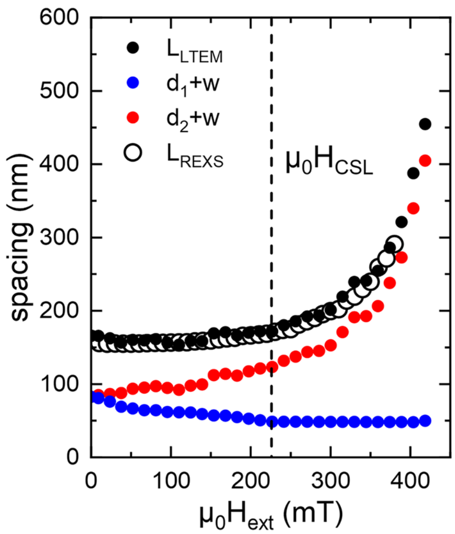

Fig. 3 | Field dependence of the modulation length and domain widths. Measured values of the stripe patterns (solid circles) obtained from an analysis of the phase patterns derived from Lorentz transmission electron microscopy (LTEM) shown in Fig. 2 as a function of the applied magnetic field, $\mu_0 H_{\mathrm{ext}}$. Plotted are the periodic length, L_{LTEM}, width of bright (dark) stripes, d_1 (d_2) including the domain wall width, w. The periodic lengths obtained from the complementary resonant elastic X-ray scattering (REXS) experiments, L_{REXS} (open circles) is also included for comparison. The vertical dashed line indicates the crossover from a π-CSL to a conventional CSL, as discussed in the subsection "Analyzing the nature of the chiral soliton lattices from real space magnetic imaging".

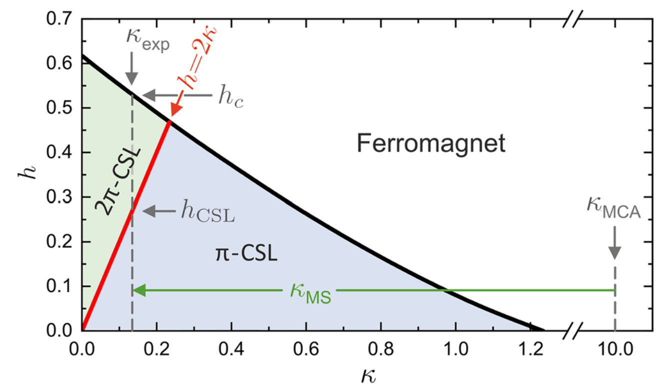

Fig. 5 | Magnetic phase diagram from the double sine-Gordon model. Ground states of $Mn_{1.4}PtSn$ as a function of the normalized magnetic field h and the normalized magnetic anisotropy κ as derived from the double sine-Gordon model. The red line separates the stability region of the π-CSL (green region) from that of the 2π-CSL (blue), while the black line indicates the transition into the saturated ferromagnetic phase, as discussed in Supplementary Note 1, "Qualitative model with anisotropy replacement", and Supplementary Note 2, "Variation of the modulation length with anisotropy".

Fig. 4 | Reciprocal-space signature of the chiral soliton lattice from resonant elastic X-ray scattering (REXS). Field dependence of (**a**) the normalized magnitude of the propagation vector and (**b**) the intensities of its 1st, 2nd, and 3rd harmonics as determined from the 1st, 2nd, and 3rd order diffraction spots in Fig. 1.

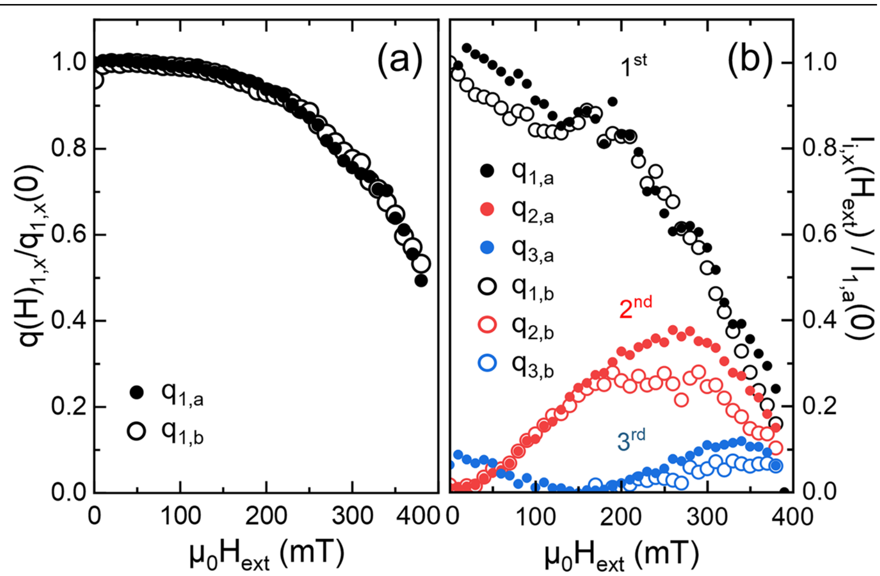

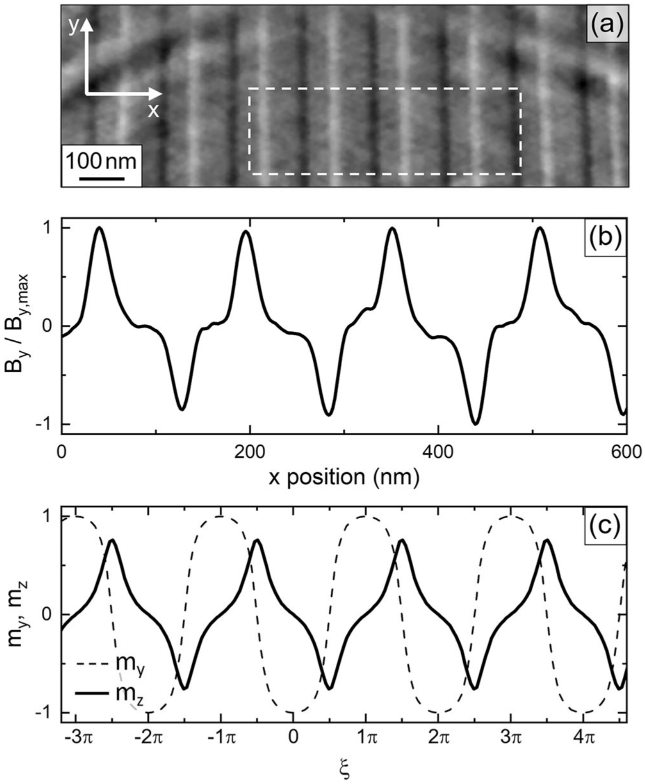

Fig. 6 | Comparison of experimental and simulated magnetization profiles at zero field. (**a**) Map of the y component of the in-plane magnetic induction, B_y, derived from the experimental Lorentz transmission electron microscopy (LTEM) image acquired at zero magnetic field [Fig. 2d]. **b** Averaged and normalized profile of the y component of the in-plane magnetic induction, $B_y(x)$, as derived from the intensity variation in the area bordered by the dashed line in (**a**). **c** Corresponding profiles of the y (solid line) and z components (dashed line) of the magnetization along a dimensionless length ξ as obtained from micromagnetic simulations.

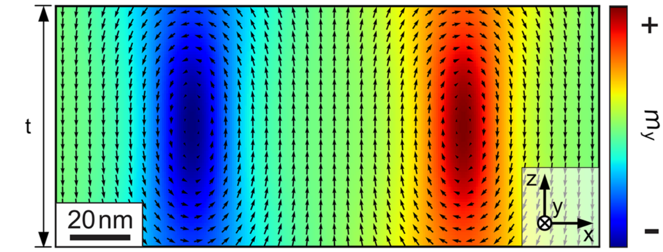

Fig. 7 | Cross-sectional view of the simulated in-plane magnetization revealing Néel-type flux-closure domains. Color map of the y component of the in-plane magnetization, $m_y(x, z)$, for a cross-section through the xz plane of the sample as obtained from micromagnetic simulations. Arrows indicate the (projected) length and orientation of the magnetization vectors in this cross-section, and t denotes the sample thickness.

strength of the shape anisotropy of $K_{MS} \simeq 0.88 K_{MCA}$, from which the critical demagnetization factor for this transition can be determined to be $N \simeq 0.68$. Assuming a cylindrical sample geometry, this translates to a length-to-diameter ratio of $\gamma \simeq 0.3$[35]—a ratio, that will be easily achieved or overcome by most bulk samples. As a consequence, the emergence of CSLs will be limited to sample geometries with high aspect ratios, as, e.g., in thin films.

However, a thorough consideration of long-range MS interactions requires to take into account the details of the sample geometry and orientation as well as that of the spin textures therein. In particular, higher-order MS effects such as spatial variation along z-direction, detailed texture profiles, and quantitative features observed in the REXS data are not captured within the effective anisotropy approximation, and will thus necessitate micromagnetic simulations.

Micromagnetic simulations. We have therefore conducted micromagnetic simulations based on the Hamiltonian described in Eq. (2) for a 1D modulation (arbitrarily chosen along x) to investigate the experimentally observed textures in the stripe domains. Computational details of the simulations are described in the "Methods" section below. In order to verify that the results of these simulations are consistent with our experimental observations, we compare in Fig. 6 the profile of the experimentally measured in-plane magnetic induction at zero magnetic field with the simulated magnetization profile. As can be seen from the solid lines in Figs. 6b, c, the normalized profiles of the experimentally determined y component of the in-plane induction, $B_y/B_y^{\max}$, and the magnetization, $m_y/|m|$, are in very good qualitative agreement. The observation that unlike for the z component, m_z [dashed line in Fig. 6c], the maxima in $m_y(\xi)$ never reach the magnitude of the full magnetic moment, $|m|$, (i.e., $\max(B_y/B_y^{\max}) < 1$) is due to the fact that identical to in the experimental situation, m_y is averaged along z over the total sample thickness. The mapping of m_y in the cross-sectional xz plane of the simulated sample in Fig. 7 reveals the occurrence of Néel-type flux-closure domains originating from magnetodipolar interactions, where the magnetic moments are partially pointing along the x direction (similar to chiral surface twists in materials with isotropic DMI[36–38]). As a consequence, and unlike in the vertical center of the sample, averaging m_y over the thickness results in a value that never reaches the magnitude of the full magnetic moment. In the experimental LTEM images, Néel-type textures remain "invisible" in out-of-plane imaging geometry, and since the intensity of the magnetic contrast in the experimental profile is normalized to its experimental maximum, $B_y/B_{y,\max}$ does reach unity in its maxima in Fig. 6b.

In a second step we investigate whether and to what extent the micromagnetic simulations also allow to describe the magnetic field-dependence of the experimental LTEM and REXS patterns. Figure 8a shows the field dependence of the periodic length, L_{sim}, and the widths of domains with moments aligned parallel ($d_2 + w$) and antiparallel to the external field ($d_1 + w$). The simulations are found to not only nicely reproduce the experimentally determined geometrical measures of the CSL stripe patterns presented in Fig. 3, also the field-dependence of the 2nd and 3rd harmonics of the propagation vector, specifically the finite value of the intensity of the 3rd harmonic at zero field and its non-monotonic course are reproduced [Figs. 4 and 8b].

The results of our micromagnetic simulations are in excellent agreement with our experimental observations. They confirm the conclusion drawn from the LTEM and REXS experiments that at low magnetic fields, the sample exhibits a π-CSL rather than a helical modulation in the ground state, which then gradually transforms to a 2π-CSL upon increasing the magnetic field.

Conclusions

We have explored in detail the magnetic textures in the Heusler compound $Mn_{1.4}PtSn$, utilizing LTEM and REXS for high-resolution real space magnetic imaging and complementary reciprocal space magnetic scattering on the very same samples and under identical conditions at room temperature. The experiments were supported by micromagnetic simulations and successive simulations of LTEM images and REXS patterns.

The basic magnetic motif in $Mn_{1.4}PtSn$, which defines both its ground state properties and its field-dependent variations, is found to be the CSL. Unlike previously discussed, the ground state is a periodic arrangement of magnetic (stripe) domains with alternating orientation along and perpendicular to the external field separated by π DWs. Due to its periodic nature and the field-induced control of the periodic length, we identify this state as a π-CSL. The LTEM and REXS experiments have consistently shown that with increasing out-of-plane magnetic field along the uniaxial

Fig. 8 | Field dependence of the soliton lattice from micromagnetic simulations. Spin textures in $Mn_{1.4}PtSn$ at finite magnetic field and anisotropy. **a** Modulation length, L_{sim} (black dots) and domain widths, $(d_{1,2} + w)_{sim}$, (red and blue dots). **b** Intensity of the first three harmonics of the propagation vector q_1, q_2, and q_3 as a function of the magnetic field determined from the spin textures resulting from micromagnetic simulations of the double sine-Gordon model with identical parameters as in (**a**).

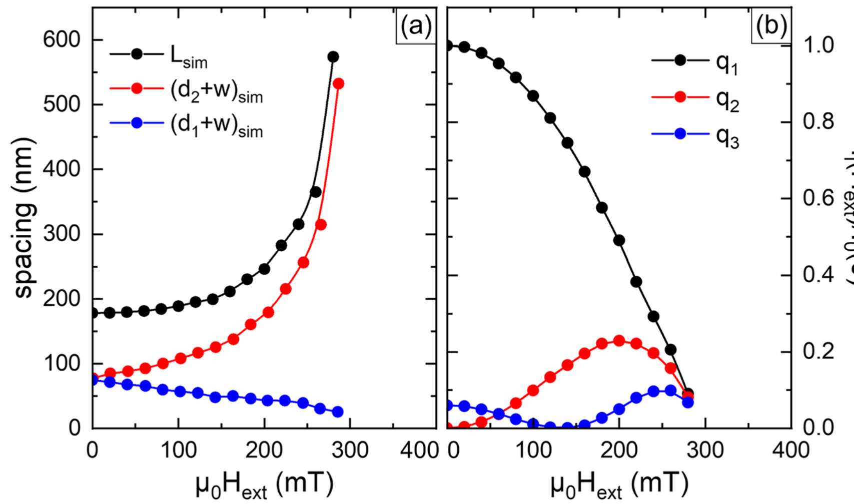

magnetocrystalline easy c axis the π-CSL eventually transforms into a "classical" 2π-CSL at a critical field $\mu_0 H_{CSL}$. Due to the anisotropic DMI, these CSLs occur in two variants of opposite chirality, the helical propagation vectors of which along the a and b directions of the crystal.

A dSG model, which takes into account the impact of both an external magnetic field and the MCA, allowed us to deduce a magnetic phase diagram that reproduces the experimentally observed π-CSL, 2π-CSL, and ferromagnetically saturated state. In the limiting cases of vanishing fields on the one hand and vanishing anisotropy on the other, the model reduces to two single sine-Gordon equations that reveal both the anisotropy-stabilized π-CSL as the magnetic ground state and its field-driven transformation into a 2π-CSL. Micromagnetic simulations based on the Hamiltonian of the dSG model further allowed us to explore the effect of the combined impact of magnetic fields and anisotropy for D_{2d} or S_4 systems and tie in closely with our experimental observations in $Mn_{1.4}PtSn$.

Crucially, this implies that the (double) sine-Gordon equation can be used as a starting point to clarify magnetic phase diagrams and to interpret transport and bulk physical properties of these structural families, independent of the specific materials details. One important and timely application will be the distinction of anomalous and topological Hall effect contributions in nanoscopic samples, where magnetometry is rarely feasible and mandatory in-situ techniques have only recently been developed[9,39,40]. It is also conceivable that this concept will inspire intuitive explanations for the formation of complex non-coplanar 2D textures like bubble lattices and antiskyrmion lattices, which have also been observed in $Mn_{1.4}PtSn$.

Methods

Experimental methods

The REXS experiments reported here were performed at beamline I10 at the Diamond Light Source (UK) using the portable octupole magnet system (POMS) end station[41]. The large wavelength at the Mn L_3 edge (637 eV, 19.5 Å) relative to the lattice spacing dictates that the experiment must be performed in transmission, i.e., with momentum transfers in the first Brillouin zone. Supplementary measurements that enabled the present insights were carried out at BL29-MaReS at ALBA (Spain). LTEM measurements were performed using a JEOL F-200 microscope. In the Lorentz mode of operation, the objective lens was used to apply magnetic fields along the axis of the microscope column, i.e., perpendicular to the sample plane. All measurements reported here were performed at room temperature.

Computational methods

Micromagnetic simulations were conducted using `Mumax`^{3} [42]. We used the following values for the exchange stiffness, Dzyaloshinskii-Moriya interaction constant, saturation magnetization, and uniaxial anisotropy constant: $A = 8 \times 10^{-12}$ J m^{-1}, $D = 4 \times 10^{-4}$ J m^{-2}, $M_S = 4.5 \times 10^5$ A m^{-1}, and $K_{MCA} = 1 \times 10^5$ J m^{-3}, respectively[5]. MS interactions were explicitly included in the simulations. The sample dimensions were set to $L_x \times 2$ nm $\times\, t$ (length × width × thickness along the x, y, and z directions, respectively). Here, L_x represents the modulation length along x as determined from energy minimization. In order to account for the fact that the determination of the lamella thickness in the FIB is easily overestimated due to the Pt protection layer, in the simulations, the thickness was adjusted to $t = 80$ nm so that the resulting periodic length at zero field matches periodic length L_{LTEM} determined from the LTEM experiments. The mesh size was set to $1 \times 1 \times 1$ nm^3, and the simulations were carried out under periodic boundary conditions in the xy plane and an open boundary condition along z.

Data availability

The datasets generated and analyzed during the current study—including LTEM micrographs, reconstructed magnetic phase maps, REXS scattering patterns, and the input/output files of the micromagnetic simulations—have been deposited in OPARA, the open access repository and archive for research data of the TUD Dresden University of Technology, where they are permanently stored and publicly accessible under the digital object identifier (DOI) https://doi.org/10.25532/OPARA-1497. Any further data are available from the corresponding authors (M. Winter, moritz.winter2@tu-dresden.de, and B. Rellinghaus, bernd.rellinghaus@tu-dresden.de) upon reasonable request; requests will be responded to within 4 weeks. There are no restrictions on data access.

Received: 2 October 2025; Accepted: 17 July 2026;
Published online: 07 August 2026

References

1. Togawa, Y. et al. Chiral magnetic soliton lattice on a chiral helimagnet. *Phys. Rev. Lett.* **108**, 107202 (2012).
2. Zhang, C. et al. Chiral helimagnetism and one-dimensional magnetic solitons in a Cr-intercalated transition metal dichalcogenide. *Adv. Mater.* **33**, 2101131 (2021).
3. Matsumura, T. et al. Chiral soliton lattice formation in monoaxial helimagnet $Yb(Ni_{1-x}Cu_x)_3Al_9$. *J. Phys. Soc. Jpn.* **86**, 124702 (2017).
4. Nayak, A. K. et al. Magnetic antiskyrmions above room temperature in tetragonal Heusler materials. *Nature* **548**, 561–566 (2017).
5. Peng, L. et al. Controlled transformation of skyrmions and antiskyrmions in a non-centrosymmetric magnet. *Nat. Nanotechnol.* **15**, 181–186 (2020).

6. Ma, T. et al. Tunable magnetic antiskyrmion size and helical period from nanometers to micrometers in a D_{2d} Heusler compound. *Adv. Mater.* **32**, 2002043 (2020).
7. Jena, J. et al. Elliptical Bloch skyrmion chiral twins in an antiskyrmion system. *Nat. Commun.* **11**, 1229 (2020).
8. Back, C. et al. The 2020 skyrmionics roadmap. *J. Phys. D Appl. Phys.* **53**, 363001 (2020).
9. Winter, M. et al. Antiskyrmions and their electrical footprint in crystalline mesoscale structures of $Mn_{1.4}PtSn$. *Commun. Mater.* **3**, 99 (2022).
10. Zuniga Cespedes, B. E., Vir, P., Milde, P., Felser, C. & Eng, L. M. Critical sample aspect ratio and magnetic field dependence for antiskyrmion formation in $Mn_{1.4}PtSn$ single crystals. *Phys. Rev. B* **103**, 184411 (2021).
11. Sukhanov, A. S. et al. Anisotropic fractal magnetic domain pattern in bulk $Mn_{1.4}PtSn$. *Phys. Rev. B* **102**, 174447 (2020).
12. Liu, Y.-R., Chen, H.-X., Chen, W., Liu, X. & Zhu, S.-L. Pentaquark and tetraquark states. *Prog. Part. Nucl. Phys.* **107**, 237–320 (2019).
13. Eto, M., Nishimura, K. & Nitta, M. Domain-wall skyrmion phase in dense QCD at strong magnetic fields using leading-order chiral perturbation theory. *Phys. Rev. Lett.* **134**, 181902 (2025).
14. Amari, Y., Nitta, M. & Yokokura, R. Spin statistics and surgeries of topological solitons in QCD matter in magnetic field. *J. High. Energy Phys.* **2025**, 171 (2025).
15. Shen, Y. & Dierking, I. Annealing and melting of active two-dimensional soliton lattices in chiral nematic films. *Soft Matter* **18**, 7045–7052 (2022).
16. Abdullah, F. A., Islam, M. T., Gomez-Aguilar, J. F. & Akbar, M. A. Impressive and innovative soliton shapes for nonlinear Konno–Oono system relating to electromagnetic field. *Opt. Quantum Electron.* **55**, 69 (2023).
17. Bogdanov, A. & Hubert, A. Thermodynamically stable magnetic vortex states in magnetic crystals. *J. Magn. Magn. Mater.* **138**, 255–269 (1994).
18. Vir, P. et al. Tetragonal superstructure of the antiskyrmion hosting Heusler compound $Mn_{1.4}PtSn$. *Chem. Mater.* **31**, 5876–5880 (2019).
19. Teague, M. R. Deterministic phase retrieval: a Green's function solution. *J. Opt. Soc. Am.* **73**, 1434–1441 (1983).
20. Zuo, C. et al. Transport of intensity equation: a tutorial. *Opt. Lasers Eng.* **135**, 106187 (2020).
21. Lubk, A. et al. Transport of intensity phase retrieval in the presence of intensity variations and unknown boundary conditions. *Optik* **319**, 172109 (2024).
22. Beg, M., Lang, M. & Fangohr, H. Ubermag: towards more effective micromagnetic workflows. *IEEE Trans. Magn.* **58**, 7300205 (2022).
23. Beleggia, M. & Zhu, Y. Electron-optical phase shift of magnetic nanoparticles I. Basic concepts. *Philos. Mag.* **83**, 1045–1057 (2003).
24. Hellwig, O., Denbeaux, G. P., Kortright, J. B. & Fullerton, E. E. X-ray studies of aligned magnetic stripe domains in perpendicular multilayers. *Phys. B* **336**, 136–144 (2003).
25. Dzyaloshinskkii, I. E. Theory of helicoidal structures in antiferromagnets. I. Nonmetals. *Sov. Phys. JETP* **19**, 960–971 (1964).
26. Bogdanov, A. & Hubert, A. The stability of vortex-like structures in uniaxial ferromagnets. *J. Magn. Magn. Mater.* **195**, 182–192 (1999).
27. Kravchuk, V. *Problems in Micromagnetism*. https://doi.org/10.13140/RG.2.2.22653.74728 (2023).
28. Condat, C. A., Guyer, R. A. & Miller, M. D. Double sine-Gordon chain. *Phys. Rev. B* **27**, 474–494 (1983).
29. Paterson, G. W. et al. Tensile deformations of the magnetic chiral soliton lattice probed by Lorentz transmission electron microscopy. *Phys. Rev. B* **101**, 184424 (2020).
30. Ross, C., Sakai, N. & Nitta, M. Exact ground states and domain walls in one dimensional chiral magnets. *J. High. Energy Phys.* **2021**, 163 (2021).
31. Karube, K. et al. Doping control of magnetic anisotropy for stable antiskyrmion formation in schreibersite $(Fe,Ni)_3P$ with s_4 symmetry. *Adv. Mater.* **34**, 2108770 (2022).
32. Sannikov, D. G. & Golovko, V. A. Different states of incommensurate phase with solitons of one and two types. *Sov. Phys. JETP* **55**, 562–565 (1982).
33. Iwabuchi, S. Commensurate-incommensurate phase transition in double sine-Gordon system. *Prog. Theor. Phys.* **70**, 941–953 (1983).
34. Izyumov, Y. A. & Laptev, V. I. Diffraction of neutrons by incommensurate magnetic structures. *Sov. Phys. JETP* **85**, 2185–2199 (1983).
35. Bozorth, R. A. & Chapin, D. M. Demagnetizing factors of rods. *J. Appl. Phys.* **13**, 320–326 (1942).
36. Leonov, A. O. et al. Chiral surface twists and skyrmion stability in nanolayers of cubic helimagnets. *Phys. Rev. Lett.* **117**, 087202 (2016).
37. Schneider, S. et al. Induction mapping of the 3D-modulated spin texture of skyrmions in thin helimagnets. *Phys. Rev. Lett.* **120**, 217201 (2018).
38. Wolf, D. et al. Unveiling the three-dimensional magnetic texture of skyrmion tubes. *Nat. Nanotechnol.* **17**, 250–255 (2022).
39. Pohl, D. et al. Probing magnetic properties at the nanoscale: in-situ Hall measurements in a TEM. *Sci. Rep.* **13**, 14871 (2023).
40. Thomas, A. et al. In-situ monitoring the magnetotransport signature of topological transitions in a chiral magnet. *Small Methods* **9**, 2401875 (2025).
41. van der Laan, G. & Figueroa, A. I. X-ray magnetic circular dichroism—a versatile tool to study magnetism. *Coord. Chem. Rev.* **277–278**, 95–129 (2014).
42. Vansteenkiste, A. et al. The design and verification of MuMax3. *AIP Adv.* **4**, 107133 (2014).

Acknowledgements

REXS was conducted using the Portable Octupole Magnet System on beamline I10 at the Diamond Light Source, UK, under proposal MM28882 and at BL29-MaReS at the ALBA Synchrotron (Spain), under proposal 20220672.

Author contributions

M.W., M.C.R., J.G., C.F. and B.R. devised the project. M.W. conducted the LTEM experiments with the help of D.P., S.S., A.Th., and D.W. M.W., M.C.R., A.S.S., B.A., J.R.B., V.U., M.V., G.vdL., and T.Hes. conducted the REXS experiments. A.P., M.A., and K.E.S. developed the theory and conducted micromagnetic simulations in close collaboration with M.W. M.W. analyzed all data. P.V., A.Ta., and M.W. prepared the samples with the support of T.Hel. M.W., B.R., M.C.R., T.Hes., A.P., M.A., and K.E.S wrote the manuscript. All authors contributed to the discussion of the results and reviewed the manuscript.

Funding

M.W. acknowledges support from the International Max Planck Research School for Chemistry and Physics of Quantum Materials (IMPRS-CPQM). M.C.R. was supported through the Emmy Noether program of the German Research Foundation, DFG, (project no. 501391385). Work at TU Dresden was supported by the DFG through CRC 1143 and the Cluster of Excellence ct.qmat (EXC 2147, project no. 390858490). K.E.S. acknowledges funding from the DFG through project no. 320163632 and through project no. 403233384 within SPP 2137. M.W., S.S., D.P., and B.R. are grateful for funding from the DFG through SPP 2137, project no. 403503416. D.P. acknowledges financial support from the DFG through project no. 504660779. S.S. acknowledges funding by the DFG within TRR404 "Active-3D" (project no. 528378584). Financial support by the EPSRC (EP/N032128/1) is gratefully acknowledged. M.A. acknowledges funding from the UDE Postdoctor Seed Funding program. Open Access funding enabled and organized by Projekt DEAL.

Competing interests

The authors declare no competing interests.

Additional information

Supplementary information The online version contains supplementary material available at https://doi.org/10.1038/s42005-026-02785-3.

Correspondence and requests for materials should be addressed to M. Winter or B. Rellinghaus.

Peer review information *Communications Physics* thanks Nitish Mathur and the other, anonymous, reviewer for their contribution to the peer review of this work.